Journal of Solid State Electrochemistry
https://doi.org/10.1007/s10008-020-04534-0

ORIGINAL PAPER

Effect of sintering temperature on electrochemical performance of porous $SrTi_{1-x}Fe_xO_{3-\delta}$ ($x = 0.35, 0.5, 0.7$) oxygen electrodes for solid oxide cells

A. Mroziński[1] · S. Molin[1] · P. Jasiński[1]

Received: 25 November 2019 / Revised: 28 February 2020 / Accepted: 28 February 2020

Abstract

This work evaluates the effects of the sintering temperature (800 °C, 900 °C, 1000 °C) of $SrTi_{1-x}Fe_xO_{3-\delta}$ ($x = 0.35, 0.5, 0.7$) porous electrodes on their electrochemical performance as potential oxygen electrode materials of solid oxide cells. The materials were prepared by a solid-state reaction method and revealed the expected cubic perovskite structure. After milling, the powders were characterised by a sub-micrometre particle size with high sinter-activity. It was shown that the lowest area specific resistance was achieved after sintering $SrTi_{0.65}Fe_{0.35}O_3$ electrodes at 1000 °C, and $SrTi_{0.5}Fe_{0.5}O_3$ and $SrTi_{0.30}Fe_{0.70}O_3$ electrodes at 800 °C, which can be considered to be a relatively low temperature. In general, EIS measurements showed that increasing the Fe content results in lowered electrode polarisation and a decrease of the series resistance. Even though the studied materials have much lower total conductivities than state-of-the-art electrode materials (e.g. $(La,Sr)(Co,Fe)O_3$), the polarisation resistances obtained in this work can be considered low.

Keywords Strontium titanate · Solid oxide cell · Oxygen electrode · Perovskite · Polarisation resistance

Introduction

Mixed ionic and electronic conducting materials (MIECs) are the main group of materials used for high temperature solid oxide cell (SOC) electrodes [1]. There are several features of porous MIEC materials that have an impact on the performance of the electrode. The microstructure of the electrode (porosity, tortuosity, particle size) [2, 3], intrinsic oxygen activity (surface exchange, oxygen diffusion) [4, 5], interface between the electrode and electrolyte or the barrier layer [6], and the electronic transport properties are all very important. The most studied group of MIEC oxygen electrode materials are the perovskites [7–9]. They are given by the general ABO_3 formula, with A being a large cation in 12-fold coordination by oxygen anions, and B a relatively smaller cation in the centre of an oxygen-coordinated octahedra (6-fold coordination). Typically, the A cation is one of the alkaline earth cations, whereas B is a transition metal cation, e.g. $CaTiO_3$—the archetypical perovskite mineral. In general, the A and B sites can be occupied by more than one cation type, thus providing enormous possibilities to develop new materials. For applications in SOCs, $(La,Sr)(Co,Fe)O_3$, LSCF, and $(La,Sr)CoO_3$, LSC, are the most studied ones [10–14]. Also, other materials groups have been studied: double perovskites, Ruddlesden-Popper-type phases [15], and others [16–21]. Typical electrode materials have high ionic and electronic conductivity levels, with total conductivities exceeding 100 S cm^{-1}; however, the exact role of the influence of the individual partial conductivity levels on the resulting electrode performance is yet to be established, and is currently an active research topic [5, 22, 23]. In this respect, materials with relatively low total conductivities (or materials with a low electronic-to-ionic conductivity ratio) and good oxygen catalyst properties are very interesting for research. Among the interesting materials with relatively low total conductivities (< 10 S cm^{-1} at 800 °C) and high ionic conductivities (comparable with yttria stabilised zirconia or ceria-based materials) are iron doped strontium titanates ($SrTi_{1-x}Fe_xO_{3-\delta}$ (STFx)) [24–27]. Because of their

Electronic supplementary material The online version of this article (https://doi.org/10.1007/s10008-020-04534-0) contains supplementary material, which is available to authorized users.

✉ A. Mroziński
aleksander.mrozinski@pg.edu.pl

[1] Faculty of Electronics, Telecommunications and Informatics, Gdansk University of Technology, ul. G. Narutowicza 11/12, 80-233 Gdansk, Poland

Published online: 06 March 2020

high ionic conductivity (~ 10^{-2} S cm^{-1} at 800 °C) [28], they have found application as oxygen separation membranes [29, 30], catalysts for water electrolysis reactions [31], resistive sensors of oxygen [32] and ethanol [33], and also in solid oxide fuel cell (SOFC) systems as electrodes [34–36] or the functional layer [37]. STFx-based materials show low polarisation resistance and good long term stability, including limited Sr surface segregation [38, 39], which is problematic for LSC/LSCF compounds.

Most studies have focussed on the properties of thin and dense STFx films used as model electrodes [24, 28], whereas the properties of porous electrodes have practically not been studied. Our previous work showed good performance of porous STF35 ($SrTi_{0.65}Fe_{0.35}O_3$) electrodes [40, 41], which has also been confirmed by other authors [38]. The obtained polarisation resistance results were comparable with the well-known LSCF electrode materials. An area specific resistance (ASR) of 0.020 Ω cm^2 at 650 °C [42] has been reported for LSCF, whereas for $SrTi_{0.1}Fe_{0.9}O_3$ (STF90), an ASR of 0.067 Ω cm^2 at 650 °C has been reported [43]. Some reports show that STFx material with $x = 0.35$ has the lowest degree of structural distortions, which makes it promising for technical applications [44] despite its relatively low electronic conductivity (~ 2 S cm^{-1}) and higher ASR values (~ 0.1 Ω cm^2 at 800 °C [40]). In general, there is only a limited number of publications related to STFx performance, and the materials require more studies.

The current work studies the effects of electrode sintering temperature on the electrochemical properties of porous $SrTi_{1-x}Fe_xO_{3-\delta}$ ($x = 0.35$, 0.5, 0.7) electrodes based on symmetrical cells. This work is a continuation of our previous initial study of an STF35 electrode [41].

Materials and methods

Material and samples preparation

$SrTi_{1-x}Fe_xO_{3-\delta}$ (STFx) materials with different Fe substitution levels ($x = 0.35$, 0.5, 0.7) were synthesised from analytical grade (> 99% purity) reagents—strontium carbonate (EuroChem, PL), titanium dioxide (EuroChem, PL), and iron (III) oxide (Chempur, PL)—by the solid-state reaction method, as described in our earlier work [41]. Briefly, stoichiometric amounts of the reagents were re-ground in an agate mortar and were subsequently ball milled (Fritsch Pulverisette 7, ZrO_2 milling container) in absolute ethanol (99.9% purity) with a rotational speed of 600 rpm for 15 h using 5 mm YSZ balls. The obtained STFx powders were further annealed at 600 °C (with a cooling/heating rate of 3 °C min^{-1}). The particle sizes of the prepared STFx powders were similar to what was shown earlier, and all powders had particles in the sub-micron range [45].

Gadolinium doped ceria (CGO) substrates, used for the preparation of the symmetrical cells, were made from a commercial powder (GDC-20 K, DKKK Japan), as presented in our previous work [41]. The surfaces of the sintered CGO substrates were ground and polished to obtain a smooth surface and remove any contaminants. After preparation, the pellets had a thickness of approximately 0.5 mm. Before the deposition of the STFx electrodes, the substrates were cleaned in acetone in an ultrasound cleaning bath.

Porous STFx electrodes were deposited on both sides of the polished CGO substrates using screen printing (DEK 65, UK). For the preparation of the pastes, an ESL403 commercial vehicle system (Electro-Science Laboratories, USA) was mixed with the prepared STFx powders in a ball mill at a mass ratio of 60:40. The mixing of the electrode pastes was carried out with a rotational speed of 200 rpm. The deposited pastes were slowly dried at 60 °C and at 130 °C. To obtain final electrodes with different microstructures, the electrodes were sintered in air at three different temperatures: 800 °C, 900 °C, and 1000 °C in a box furnace (Carbolite RHF1600, UK). Each dried electrode was heated up to 600 °C (for 1 h with a ramp of 1.5 °C min^{-1}) in order to fire the binder, and then dwelled for 2 h at the appropriate temperature, with heating and cooling ramps of 3 °C min^{-1}. The prepared electrodes had an active area of 0.4 cm^2. For electrical contact, the electrodes were brush-painted with Pt paste (ESL 5542, Electro-Science Laboratories, USA), dried, and pre-sintered at 600 °C.

Microstructure and performance analysis

The X-ray diffractometry (XRD) technique was used to determine the phase composition of the fabricated STFx powders. Measurements were performed at room temperature in the air using a Bruker D2 Phaser with an XE-T detector.

The investigation of the linear thermal expansion was carried out using a Netzsch DIL402 dilatometer. The STFx powders were formed into cylinders and heat up to 1100 °C with a heating rate of 5 °C min^{-1}, dwelled for 15 min, and then cooled at a rate of 3 °C min^{-1}. The procedure was carried out in 21% O_2.

A Phenom XL (Thermo Fisher Scientific, the Netherlands) scanning electron microscope (SEM) was used for imaging of the polished cross sections of the symmetrical cells. All SEM images were made using a backscattered electron (BSE) detector with an applied accelerating voltage of 10 kV in a 0.1 Pa vacuum. The chemical compositions of the investigated electrodes were determined via energy-dispersive X-ray (EDX) spectroscopy using an integrated analyser (Thermo Fisher Scientific, 25 mm^2 Silicon Drift Detector) with an accelerating voltage of 20 kV.

Electrochemical impedance spectroscopy (EIS) studies were carried out using a Novocontrol Alpha-A mainframe with a 4-wire ZG4 interface. In order to study, the impact of

the sintering temperature on the ASR, the STFx symmetrical samples were measured in a spring-based compression cell in flowing air. For electrical contact, gold meshes were used for contacting the samples. The measurement parameters were used as described in our previous work [41].

The DRTTools Matlab GUI, available from prof. Ciucci's group, was used for the analysis of the distribution of relaxation times [46, 47].

Results and discussion

Materials characterisation

The phase composition of the powders prepared by the solid-state reaction method was studied using X-ray diffractometry. The XRD of the prepared powders showed the formation of the expected cubic perovskite phase (*Pm*3*m*), in agreement with the crystallographic database (Inorganic Crystal Structure Database #18-6710). The inset of Fig. 1a) shows the change in peak position for powders with different iron contents. With an increasing Fe content, the peaks shift towards higher 2θ angles, indicating the decrease of the unit cell size. The ionic radii (for coordination number 6) of Fe^{3+} was 0.55 Å (in the low spin state), whereas for the Ti^{4+}, it was 0.605 Å.

The general microstructure of an exemplary symmetrical sample (STF50) is presented in Fig. 1b. The low magnification image shows a uniform electrode thickness of ~25–30 μm over the electrolyte surface. On top of the porous electrode, a painted Pt current collector has a thickness of ~10 μm. The CGO substrate has a thickness of ~500 μm, which varies between 450 and 600 μm for all studied samples.

The sintering and thermal expansion properties of STFx materials were evaluated by dilatometry. Figure 1c presents the results of the sintering part of the measurement, whereas the inset shows the thermal expansion part (after the sintering). Upon heating, high thermal expansion of the STF70 compound is visible. The sintering behaviour of the samples is strongly dependent on the iron content. A higher iron content results in lower onset temperature of sintering and higher shrinkage during the dwelling stage (at 1100 °C). The sintering onset temperatures for the STF35 and STF50 were ~690 °C and for the STF70 ~680 °C. The total shrinkages of the pellets after the dilatometry study was 17%, 21%, and ~25% for STF35, STF50, and STF70, respectively.

Thermal expansion coefficients (TEC) were determined based on the cooling stage of dilatometry. For STF35, STF50, and STF70, values of ~16, ~18, and ~23 × 10^{-6} K^{-1} were obtained (in the temperature range 1000 °C–RT), respectively. The addition of iron increases the TEC considerably (possibly including the contribution of chemical expansion), which can make practical application of iron-rich samples troublesome. For example, the TEC of the CGO substrate is ~12–13 × 10^{-6} K^{-1} [48]; therefore, large stresses will be generated between the TEC-dissimilar materials.

The porosities of the cylindrical samples sintered at 1100 °C were measured by the Archimedes method. Porosities of 29%, 23%, and 5% were obtained for STF35, STF50, and STF70, respectively. The dilatometry and porosity measurement results show that increasing the iron content results in improved sinterability, but also results in an increased TEC.

Electrochemical characterisation

For the evaluation of the electrochemical performance towards the oxygen reduction/oxidation reaction (ORR/OER) of the STFx materials, electrochemical impedance spectroscopy (EIS) measurements were carried out. Samples with symmetrical electrodes were prepared on ionic conducting CGO and were sintered at either 800 °C, 900 °C, or 1000 °C. The symmetrical electrodes were measured by EIS in the air in the temperature range of 800 °C to 500 °C with 50 °C decrements. The EIS data were standardised for a specific surface of the electrodes by using the formulas: $R_s = R_{ohm} \times A$ and

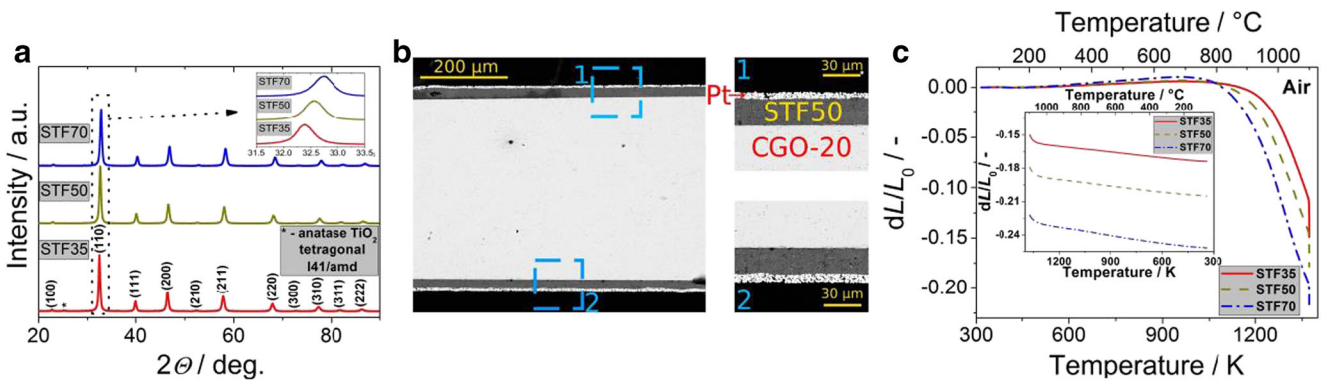

Fig. 1 **a** X-ray diffractometry of the fabricated powders, **b** SEM images of polished cross sections of an exemplary symmetrical cell with porous electrodes, and **c** sintering/thermal expansion curves of STF35, STF50, and STF70

ASR $= \frac{R_{pol} \times A}{2}$, where R_s is the series resistance, R_{ohm} is the measured ohmic resistance, R_{pol} is the polarisation resistance, and A is the area of the electrodes (0.4 cm^2).

The electrode responses, given by the ASR values, are directly comparable and represent the electrochemical performance of the electrodes, influenced by the sintering and physico-chemical material properties. In the case of comparison of the R_s values, the values are also influenced by the CGO thickness, which varies between the samples.

It is worth noting that the R_s and ASR values were stable during the few hours of measurement, i.e. no degradation nor activation of the electrodes was noted in the few hours of isothermal holds.

Figure 2 presents the impedance spectra of the differently sintered electrodes measured at 700 °C. A similar plot for the measurement temperature of 800 °C can be found in the Supplementary materials (Fig. S1). Also, Fig. S2 in the Supplementary materials provides the impedance spectra of STFx materials sintered at 800 °C measured at different temperatures (700 °C, 750 °C, and 800 °C). For comparison of the impedance values, the scaling of the axes is the same. The values of R_s and ASR depend on the sintering temperature to different extents, depending on the sample composition. Clearly, there is a visible effect of the sintering temperature on the electrochemical performance of the electrodes. Based on the measured impedance spectra, the values of R_s and ASR were plotted collectively on an Arrhenius scale. The results presented in Fig. 3 are as follows: R_s of STF35, STF50, and STF70 in Fig. 2a–c and ASR in Fig. 3d–f, respectively.

By analysing the R_s values obtained for the three studied materials as a function of the temperature, differences can be observed, which are in-line with the impedance spectra shown in Fig. 2. For STF35 and STF50, increasing the sintering temperature decreases R_s. This effect is strong for the STF35 sample and still noticeable for the STF50. For STF70, a slight increase of R_s is observed. These results might be connected to the electronic conductivity of the materials, and possible current restriction at the interface or ohmic resistance of the porous electrodes. STF70 has the highest total conductivity, so the possible current restriction will be the lowest. A rough calculation of the ohmic contribution of the porous electrodes based on the electrical conductivity of CGO results in relatively low R_s values of STFx, i.e. for the least conductive porous STF35 at 800 °C, the series resistance addition would be only ~ 10 mΩ cm^2. For comparison, the ohmic resistance introduced by a 550 μm thick CGO substrate is estimated to be ~ 400 mΩ cm^2 (based on the $Ce_{0.8}Gd_{0.2}O_{2-\delta}$ conductivity value of 0.140 S cm^{-1} at 800 °C [49, 50]). The activation energy of series resistance for all STFx symmetric samples is ~ 0.67 eV, which is in line with values for doped ceria compounds [51].

Interestingly, the ASR values of the STF35 electrode are practically independent of the sintering temperature and have values of ~ 70 mΩ cm^2 at 800 °C. The same effect was observed in our previous study [41]. For STF50 and STF70, the ASR values are dependent on the sintering temperature, reaching the lowest values for electrodes sintered at 800 °C. Especially for STF70, the increase of the sintering temperature leads to a large increase of the ASR. For STF50 and STF70 electrodes processed and measured at 800 °C, the ASR values are ~ 30 mΩ cm^2 and ~ 22 mΩ cm^2, respectively. The obtained values can be considered very low and are comparable with the best performing mixed conducting oxygen electrodes, such as LSC, LSCF, and others. The very best reported electrodes outperform the STFx electrodes studied in this work, but it is still interesting that electrodes with relatively low total conductivity have such good performance. The activation energy of polarisation resistance is very similar for all STFx materials (~ 1.29–1.24 eV) with a small tendency to decrease with increasing the Fe content.

The polarisation resistances obtained for Co-free cathodes were summarised by Hashim et al. [52]. The lowest reported

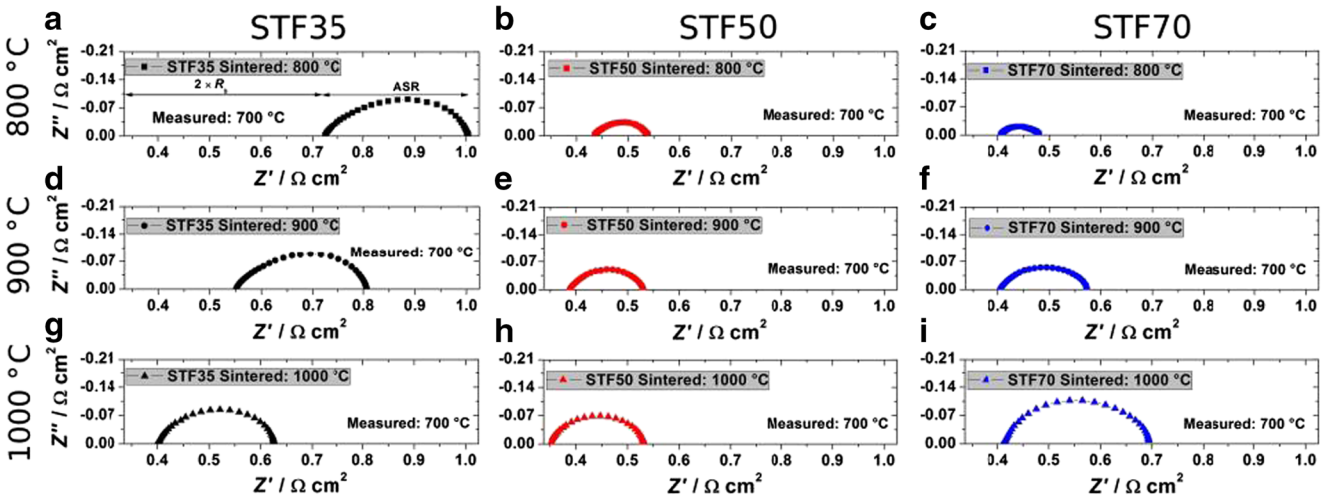

Fig. 2 Impedance spectra of STFx materials sintered at different temperatures (800 °C/900 °C/1000 °C), measured at 700 °C in 21% O_2

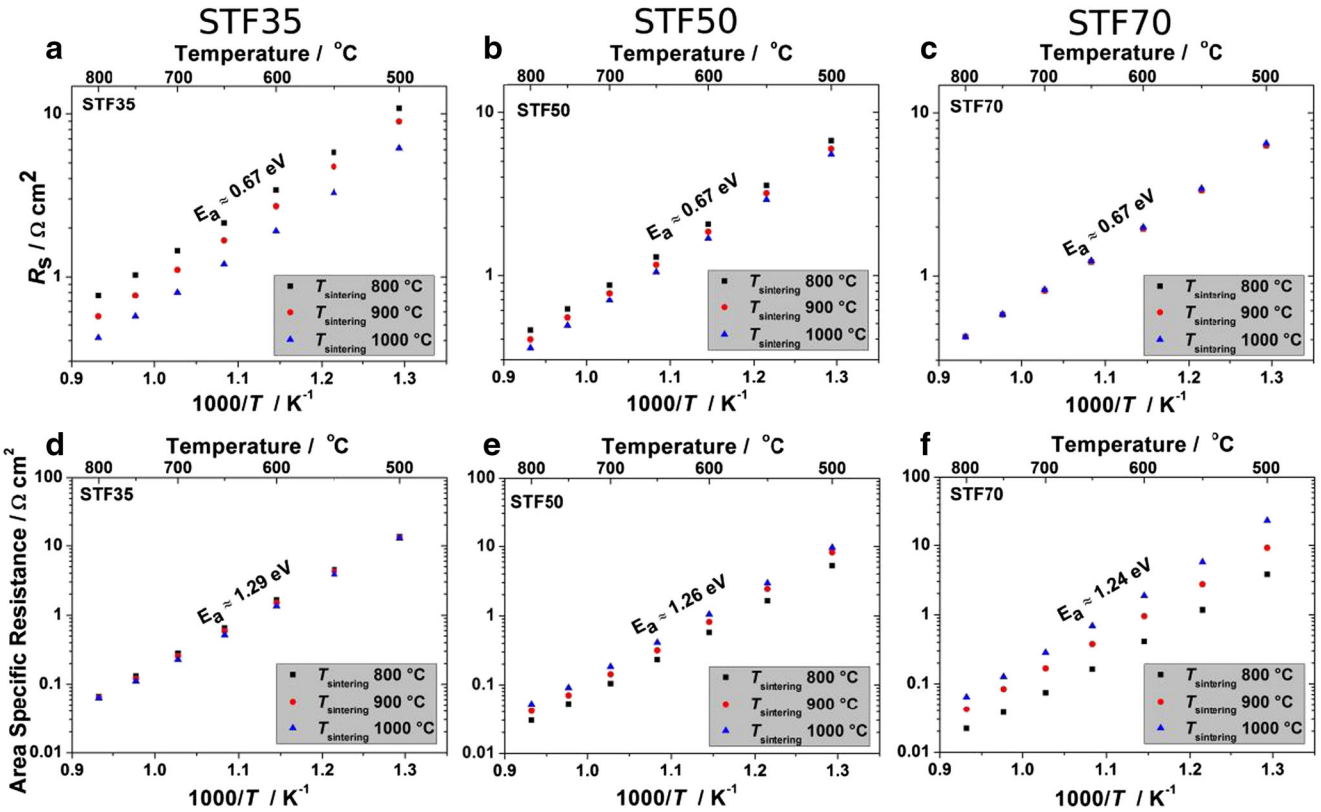

Fig. 3 Series (**a**–**c**) and polarisation (**d**–**f**) resistances of the symmetrical STF35, STF50, and STF70 electrodes, respectively, sintered at different temperatures (800 °C/900 °C/1000 °C) as a function of temperature in 21% O_2

polarisation resistance values were obtained for $PrBa_{0.97}Fe_2O_{5+d}$ and were as low as 0.019 Ω cm^2. The results obtained in this work for STFx lie within the range of the best materials reported. Furthermore, STFx materials can be easily modified to enhance their electrocatalytic activity, e.g. by partial Co substitution [25].

To further evaluate the influence of the sintering temperature on the electrode performances, distribution of relaxation times (DRT) analyses of their spectra were performed. DRT analysis is a powerful tool to investigate electrochemical processes [53–56]. The results of the DRT analysis of the spectra shown in Fig. 2 are presented in Fig. 4. Additionally, the results of the DRT analysis of samples sintered at 800 °C and measured at three different temperatures (700 °C, 750 °C, and 800 °C) are provided in Fig. S3 in the Supplementary materials. These analyses are mostly used to support the selection of the proper sintering temperature of the STFx electrodes and do not fully explain the occurring electrode processes, which will be the aim of our future work.

For all electrodes, increasing the sintering temperature results in a shift of the characteristic frequencies towards lower values. To begin with, all spectra show a distinct high frequency contribution (f_{HF}~1000 Hz). For STF35, it decreases with increased sintering temperature, also shifting towards lower frequencies. STF50 shows quite similar behaviour, but to a smaller extent. For STF70, the contributions do not change much and have a constant characteristic frequency.

Besides the high frequency contribution, which is well separated in the DRT spectra, there are at least two lower frequency contributions that can be analysed. For STF35, the electrode resistance (given the area under the DRT plot) is similar for all temperatures, with a slightly lower value after sintering at 1000 °C. The main difference between the low and high temperature sintered STF35 materials is the medium frequency contribution ($f_{MF(800\ °C)}$~500 Hz), which has the highest resistance for the electrode sintered at 800 °C. Nevertheless, the lower frequency process ($f_{LF(800\ °C)}$~50 Hz) dominates over the entire spectrum. For STF50 and STF70 electrodes, the spectra are very similar for all sintering temperatures, but the magnitude changes. An increase of the sintering temperature results in decreased electrode performance. All electrode processes seem to increase their resistance. For STF50, the dominating contribution is the low frequency process at all temperatures ($f_{LF(800\ °C)}$~80 Hz, $f_{LF(1000\ °C)}$~20 Hz). STF70 shows different behaviour. For electrode sintered at 800 °C, the dominating process is the medium frequency process ($f_{MF(800\ °C)}$~150 Hz), whereas for higher sintering temperatures, the low frequency process dominates ($f_{MF(1000\ °C)}$~10 Hz). For STF70 electrodes sintered at 900 °C and 1000 °C, an additional contribution at even lower

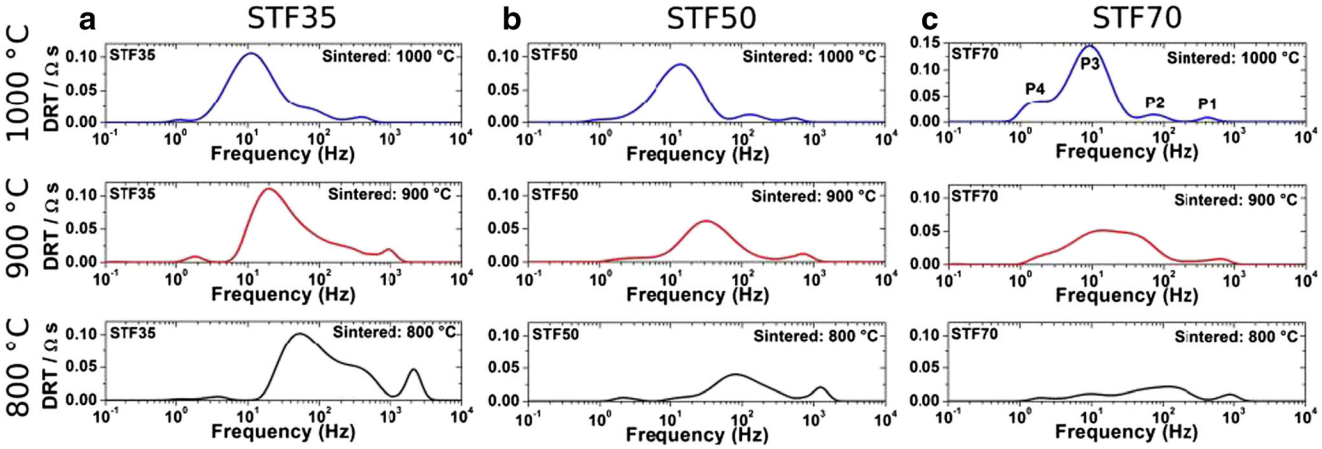

Fig. 4 Exemplary distribution of relaxation times plots of impedance of symmetrical STF35 (**a**), STF50 (**b**), and STF70 (**c**) electrodes measured at 700 °C at 21% O_2, as a function of sintering temperature (800 °C/900 °C/1000 °C)

frequencies becomes apparent. As the electrode microstructure densifies, the porosity becomes lower and the gas diffusion impedance becomes measurable, which agrees well with the characteristic frequency of 1–4 Hz.

The electrochemical processes occurring at the electrodes/interfaces, which have been assigned qualitatively to the peaks from the DRT spectra (based on our previous study and the specific frequencies/capacitances of the processes) are summarised as follows:

P1—(~ 1000 Hz) STFx-CGO interface contribution;
P2—(80–200 Hz) potential Gerischer element: oxygen diffusion in the bulk of the particles;
P3—(10–30 Hz) non-dissociative adsorption/charge transfer;
P4—(~1 Hz) gas diffusion.

The provided description is only a general overview of the possible processes. A more detailed discussion, including studies of the pO_2/temperature dependence of the contributions, will be given in the future. For example, Zhang et al. [38] recently studied STFx materials and used an equivalent circuit consisting of two components. Thus further studies are required to clarify the underlying mechanisms, which are needed to understand the behaviour of mixed ionic-electronic conductors.

In general, the oxygen reduction/oxidation performance increases with increasing iron content. When titanium (Ti^{4+}) is substituted for iron, it can either have a + 3 or + 4 oxidation state. The specific ratio of the cations will depend on the atmosphere and overpotentials. In the case of the formation of Fe^{3+}, charge compensation occurs by the generation of electron holes in the valence bands or, predominantly, by the formation of oxygen vacancies [57]. Either way, both effects should be positive for the performance of mixed ionic-electronic conductors. For Fe-rich compositions, the effective band gap is drastically reduced, the materials become "electron-rich", and the resulting availability of electrons for oxygen reduction is much higher. The surface exchange coefficient for STF70 is orders of magnitude higher than for pure or slightly Fe-doped $SrTiO_3$ [57–59].

As previously reported by Jung and Tuller [28], based on a thin film study, STFx (for x between 0.05 and 0.80) most probably have a common limiting process. The authors describe it as a surface oxygen exchange, occurring at the surface of the electrode materials. This explanation was

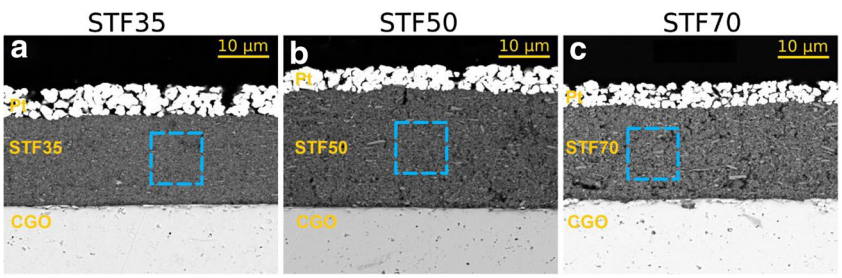

Fig. 5 Post-mortem SEM images of the polished cross section of the symmetrical cells with the STF35 (**a**), STF50 (**b**), and STF70 (**c**) porous electrodes sintered at 800 °C. Regions marked by the dashed squares were analysed by EDS to determine their chemical compositions (results are included in Table 1)

Table 1 EDX results for the STF35, STF50, and STF70 cathodes sintered at 800 °C expressed at percentage of atomic mass

	Sr/%	Ti/%	Fe/%	O/%	Ti: Fe	Sr: (Ti + Fe)
Area STF35	17.7	11.7	6.2	64.4	1.89	0.99
Area STF50	18.7	9.6	9.2	62.5	1.04	0.99
Area STF70	18.8	5.9	13.3	62.1	0.44	0.98
Point 1	15.1	7.1	6.9	71	1.02	1.08
Point 2	16.5	8.5	8.3	66.7	1.03	0.99
STF35 powder	17.1	11.7	5.7	65.5	2.05	0.98
STF50 powder	17.3	9.6	8.1	64.9	1.19	0.98
STF70 powder	14.9	5.1	11.1	68.9	0.46	0.92

further confirmed by subsequent works. Metlenko et al. [60] have studied the oxygen diffusion and surface exchange of STFx materials. They concluded that oxygen diffusion occurs via vacancy migration and that the oxygen diffusivity increases continuously as a function of iron concentration. In addition, the authors support the claim that the oxygen surface exchange occurs by one single mechanism for electron-poor and electron-rich materials. The authors proposed that the energy levels of oxygen adsorbates at the oxide surface, relative to the energy of the conduction-band edge, play a key role in the process.

Comparing the performance of the STFx materials studied in this work with other materials reveals good performance, especially for the Fe-rich compound. The polarisation level achieved for this electrode (~ 20 mΩ cm^2 at 800 °C, ~ 0.41 Ω cm^2 at 600 °C) is comparable with the performance of LSCF (~ 12 mΩ cm^2 at 800 °C); see Fig. S4 in Supplementary materials. State-of-the art LSC electrodes show initial performance at a level of ~ 100 mΩ cm^2 at 600 °C [61, 62], but the results vary greatly. Molin et al. studied STF35 and STF50 deposited on YSZ and reported ASR_{pol} values of ~ 120 mΩ cm^2 at 800 °C [40]. Zhang et al. have shown high performance and stability of STF70 electrodes of 30 mΩ cm^2 at 800 °C and ~ 0.4 Ω cm^2 at 600 °C. Our results, especially for STF70 sintered at 800 °C, thus show very high performance.

Based on the literature findings, it would be interesting to study whether it is possible to further improve the performance of STFx, e.g. by the introduction of surface catalysts (either primarily electronic/ionic, or mixed conducting), for example by an infiltration technique (and to what extent) [63, 64]. This work establishes the selection of sintering conditions and baseline measurements for future work, including infiltration and chemical modification of the compositions.

Microstructure analysis

Post-mortem SEM images of the porous STF35/50/70 electrodes sintered at 800 °C are presented in Fig. 5. A microstructure comparison of the STFx samples sintered at 800 °C, 900 °C, and 1000 °C is provided in Fig. S5 in the Supplementary materials. For each of the electrodes, the chemical composition was analysed using EDS analysis of the centre part of the electrodes (regions marked by dashed squares). The EDX results are presented in Table 1 and are in good agreement with the desired stoichiometries.

As can be seen in Fig. 6, the electrodes have uniform thicknesses between 20 and 30 μm. No cracks or other defects were detected. The morphology of the electrodes is similar: small grains of the synthesised STFx materials result in small pores and a large surface area available for the electrochemical reaction. The prepared Pt contact layer has a thickness of ~ 5–10 μm and serves the role of the current collector. The use of the current collector is required due to the relatively low electronic conductivity of STF35, for which the results have been observed to depend on the contact area of the current collector, indicating current constriction effects. For 20–30 μm thick STFx electrodes, the catalytic activity of the Pt contact layer is negligible; it only serves as a metallic-conducting contact layer.

For the STF50 sample sintered at 800 °C, a linear scan elemental analysis was performed across the Pt/porous electrode/CGO substrate layers. Line scan results, including Pt, Sr, Ti, Fe, Ce, and Gd, are shown in Fig. 6. The strontium profile shows a small but noticeable gradient, with less strontium at

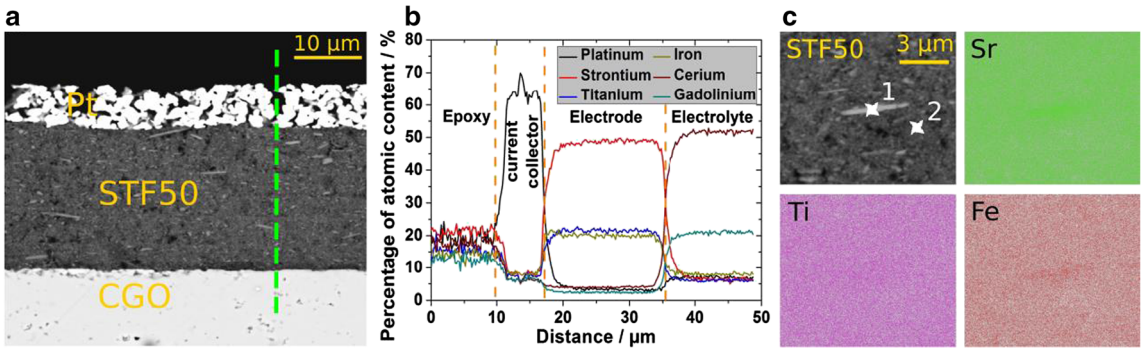

Fig. 6 SEM images of polished cross section of the porous STF50 electrode (**a**) investigated by EDS analysis: line (**b**), point and mapping (**c**)

the CGO/STF50 interface and more at the Pt/STF50 interface. Titanium is distributed uniformly throughout the thickness of the porous electrode; however, at the CGO/STF50 interface, a marked increase of Ti content is detected. The profile of iron shows an opposite trend to strontium; the amount of Fe increases towards the CGO/STF50 interface. Even though the processing and measurement temperature did not exceed a relatively low temperature of 800 °C, there is some visible cation diffusion already causing visible differences in the chemical composition.

Throughout the electrode material, some elongated particles can be seen, especially in the STF50 and STF70 samples. These platelet/rod-like particles were analysed by SEM/EDS in more detail, as presented in Fig. 6c and Fig. S6 in the Supplementary materials. The surrounding regular particles have very small particle sizes, well below 1 μm, whereas the length of this particular elongated particle reaches 10 μm. The chemical composition of the particles was analysed by EDS. Elemental maps (Fig. 6c) did not reveal any noticeable chemical composition difference, confirmed further by point analyses (points 1 and 2 in Fig. 6c), shown in Table 1. A slight increase in Sr in relation to Ti/Fe is the only difference between the particles, but it is possible that this deviation is rather small. The presence of these particles might originate from the mechanical milling step. They were not detected in the as-synthesised powders. Reports exist of STFx powder synthesis by mechanical alloying methods, suggesting their potential for reactions/deformation under mechanical loads. Nonetheless, due to the similar chemical composition, the elongated particles are not supposed to be harmful for the electrode performance.

Conclusions

Three different compositions of $SrTi_{1-x}Fe_xO_{3-\delta}$ ($x = 0.35$, 0.5, 0.7) were fabricated by solid-state reaction method and were analysed for their electrochemical performance depending on the sintering temperature. EIS measurements were analysed in terms of series (ohmic) and polarisation (ASR) contributions. For the three studied electrodes, the lowest ASR values were obtained for STF35 sintered at 1000 °C and for STF50 and STF70 when sintered at only 800 °C. The results show that iron has a strong effect on the electrode performance: the iron-rich sample showed high sinter-activity and low ASR ~ 20 mΩ cm^2 at 800 °C (obtained only for the electrode sintered at 800 °C). DRT analysis of the processes showed that STF70 differs from STF35 and STF50 in terms of the low frequency contribution, attributed to the adsorption of oxygen on the catalyst surface.

This work establishes the optimised sintering conditions of the studied powders. The studies will be further extended with a detailed EIS-DRT analysis, and the effects of surface modifications on the performance will be studied.

Funding information This work was supported by the "Understanding and minimisation of ohmic and polarisation losses in solid oxide cells by nanocrystalline ceramic and cermet functional layers" project funded by the National Science Centre, Poland, based on decision 2017/25/B/ST8/02275.

References

1. Baharuddin NA, Muchtar A, Somalu MR (2017) Short review on cobalt-free cathodes for solid oxide fuel cells. Int J Hydrog Energy 42:9149–9155
2. Rheinheimer W, Phuah XL, Wang H et al (2019) The role of point defects and defect gradients in flash sintering of perovskite oxides. Acta Mater 165:398–408
3. Rolle A, Mohamed HAA, Huo D et al (2016) Ca 3 Co 4 O 9 + δ , a growing potential SOFC cathode material: impact of the layer composition and thickness on the electrochemical properties. Solid State Ionics 294:21–30
4. Rolle A, Boulfrad S, Nagasawa K et al (2011) Optimisation of the solid oxide fuel cell (SOFC) cathode material Ca 3Co4O9-δ. J Power Sources 196:7328–7332
5. Perry NH, Kim JJ, Tuller HL (2018) Oxygen surface exchange kinetics measurement by simultaneous optical transmission relaxation and impedance spectroscopy: Sr(Ti,Fe)O $_{3-x}$ thin film case study. Sci Technol Adv Mater 19(1):130–141
6. Szymczewska D, Karczewski J, Chrzan A, Jasinski P (2017) CGO as a barrier layer between LSCF electrodes and YSZ electrolyte fabricated by spray pyrolysis for solid oxide fuel cells. Solid State Ionics 302:113–117
7. Tsipis EV, Kharton VV (2011) Electrode materials and reaction mechanisms in solid oxide fuel cells: a brief review. III Recent trends and selected methodological aspects. J Solid State Electrochem 15:1007–1040
8. Zhang Y, Knibbe R, Sunarso J et al (2017) Recent progress on advanced materials for solid-oxide fuel cells operating below 500 °C. Adv Mater 29:1–33
9. Zhang WW, Chen M, Povoden-Karadeniz E, Hendriksen PV (2016) Thermodynamic modeling of the Sr-Co-Fe-O system. Solid State Ionics 292:88–97
10. Muhammed Ali SA, Anwar M, Mahmud LS et al (2019) Influence of current collecting and functional layer thickness on the performance stability of La 0.6 Sr 0.4 Co 0.2 Fe 0.8 O 3-δ -Ce 0.8 Sm 0.2 O 1.9 composite cathode. J Solid State Electrochem 23:1155–1164
11. Jiang SP (2019) Development of lanthanum strontium cobalt ferrite perovskite electrodes of solid oxide fuel cells – a review. Int J Hydrog Energy 44:7448–7493

12. Kivi I, Aruväli J, Kirsimäe K et al (2017) Influence of humidified synthetic air feeding conditions on the stoichiometry of $(La_{1-x}Sr_x)_yCoO_{3-\delta}$ and $La_{0.6}Sr_{0.4}Co_{0.2}Fe_{0.8}O_{3-\delta}$ cathodes under applied potential measured by electrochemical in situ high-temperature XRD method. J Solid State Electrochem 21:361–369
13. Kogler S, Nenning A, Rupp GM et al (2015) Comparison of electrochemical properties of La0.6Sr0.4FeO3.δ; thin film electrodes: oxidizing vs. reducing conditions. J Electrochem Soc 162:F317–F326
14. Muhammed Ali SA, Anwar M, Baharuddin NA et al (2018) Enhanced electrochemical performance of LSCF cathode through selection of optimum fabrication parameters. J Solid State Electrochem 22:263–273
15. Garali M, Kahlaoui M, Mohammed B et al (2019) Synthesis, characterization and electrochemical properties of La2-xEuxNiO4+Δ Ruddlesden-Popper-type layered nickelates as cathode materials for SOFC applications. Int J Hydrog Energy 44:11020–11032
16. Nicollet C, Flura A, Vibhu V et al (2016) Preparation and characterization of Pr2NiO4+δ infiltrated into Gd-doped ceria as SOFC cathode. J Solid State Electrochem 20:2071–2078
17. Niemczyk A, Olszewska A, Du Z et al (2018) Assessment of layered La 2-x (Sr,Ba) x CuO 4-Δ oxides as potential cathode materials for SOFCs. Int J Hydrog Energy 43:15492–15504
18. Philippeau B, Mauvy F, Nicollet C et al (2015) Oxygen reduction reaction in Pr2NiO4+δ/Ce0.9Gd0.1O1.95 and La0.6Sr0.4Co0.2Fe0.8O3−δ/La0.8Sr0.2Ga0.8Mg0.2O2.80 half cells: an electrochemical study. J Solid State Electrochem 19:871–882
19. Zhu L, Hong T, Xu C, Cheng J (2019) A novel dual phase BaCe0.5Fe0.5O3-Δ cathode with high oxygen electrocatalysis activity for intermediate temperature solid oxide fuel cells. Int J Hydrog Energy 44:15400–15408
20. Gao Z, Ding X, Ding D et al (2018) Infiltrated Pr2NiO4 as promising bi-electrode for symmetrical solid oxide fuel cells. Int J Hydrog Energy 43:8953–8961
21. Li H, Sun LP, Feng Q et al (2017) Investigation of Pr 2 NiMnO 6 - Ce 0.9 Gd 0.1 O 1.95 composite cathode for intermediate-temperature solid oxide fuel cells. J Solid State Electrochem 21:273–280
22. Yoo C-Y, Bouwmeester HJM (2012) Oxygen surface exchange kinetics of SrTi1−xFexO3−δ mixed conducting oxides. Phys Chem Chem Phys 14:11759
23. Perry NH, Ishihara T (2016) Roles of bulk and surface chemistry in the oxygen exchange kinetics and related properties of mixed conducting perovskite oxide electrodes. Materials (Basel) 9:1–24
24. Jung W, Tuller HL (2008) Investigation of cathode behavior of model thin-film SrTi[sub 1−x]Fe[sub x]O[sub 3−δ] (x=0.35 and 0.5) mixed ionic-electronic conducting electrodes. J Electrochem Soc 155:B1194–B1201
25. Zhang SL, Wang H, Lu MY et al (2018) Cobalt-substituted SrTi0.3Fe0.7O3?d: a stable high-performance oxygen electrode material for intermediate-temperature solid oxide electrochemical cells. Energy Environ Sci 11:1870–1970
26. Yao C, Zhang H, Liu X et al (2019) A niobium and tungsten co-doped SrFeO 3-δ perovskite as cathode for intermediate temperature solid oxide fuel cells. Ceram Int 45:7351–7358
27. Fan L, Zhu B, Su PC, He C (2018) Nanomaterials and technologies for low temperature solid oxide fuel cells: recent advances, challenges and opportunities. Nano Energy 45:148–176
28. Jung W, Tuller HL (2009) Impedance study of SrTi1-xFexO3-δ (x = 0.05 to 0.80) mixed ionic-electronic conducting model cathode. Solid State Ionics 180:843–847
29. Oliveira Silva R, Malzbender J, Schulze-Küppers F et al (2017) Mechanical properties and lifetime predictions of dense SrTi1-xFexO3-δ(x = 0.25, 0.35, 0.5). J Eur Ceram Soc 37:2629–2636
30. Liu Y, Baumann S, Schulze-Küppers F et al (2018) Co and Fe co-doping influence on functional properties of SrTiO3for use as oxygen transport membranes. J Eur Ceram Soc 38:5058–5066
31. Hayden BE, Rogers FK (2018) Oxygen reduction and oxygen evolution on SrTi1 − xFexO3 − y (STFO) perovskite electrocatalysts. J Electroanal Chem 819:275–282
32. Song JL, Guo X (2015) SrTi<inf>0.65</inf>Fe<inf>0.35</inf>O<inf>3</inf> nanofibers for oxygen sensing. Solid State Ionics 278:26–31
33. Sarin N, Mishra M, Gupta G et al (2018) Elucidating iron doping induced n- to p- characteristics of strontium titanate based ethanol sensors. Curr Appl Phys 18:246–253
34. Zhu T, Fowler DE, Poeppelmeier KR et al (2016) Hydrogen oxidation mechanisms on perovskite solid oxide fuel cell anodes. J Electrochem Soc 163:F952–F961
35. Łącz A, Drożdż E (2019) Porous Y and Cr – doped SrTiO 3 materials — electrical and redox properties. J Solid State Electrochem 23:2989–2997
36. Nenning A, Volgger L, Miller E et al (2017) The electrochemical properties of $Sr(Ti,Fe)O_{3-\delta}$ for anodes in solid oxide fuel cells. J Electrochem Soc 164:F364–F371
37. Chrzan A, Karczewski J, Gazda M et al (2015) Investigation of thin perovskite layers between cathode and doped ceria used as buffer layer in solid oxide fuel cells. J Solid State Electrochem 19:1807–1815
38. Zhang S-L, Cox D, Yang H et al (2019) High stability SrTi 1−x Fe x O 3−δ electrodes for oxygen reduction and oxygen evolution reactions. J Mater Chem A:21447–21458
39. Cao Z, Fan L, Zhang G et al (2019) Titanium-substituted ferrite perovskite: an excellent sulfur and coking tolerant anode catalyst for SOFCs. Catal Today 330:217–221
40. Molin S, Lewandowska-Iwaniak W, Kusz B et al (2012) Structural and electrical properties of $Sr(Ti, Fe)O_{3-\delta}$ materials for SOFC cathodes. J Electroceram 28:80–87
41. Mroziński A, Molin S, Karczewski J et al (2019) Electrochemical properties of porous $Sr_{0.86}Ti_{0.65}Fe_{0.35}O_3$ oxygen electrodes in solid oxide cells: impedance study of symmetrical electrodes. Int J Hydrog Energy 44:1827–1838
42. Çelikbilek Ö, Jauffres D, Dessemond L et al (2016) A coupled experimental/numerical approach for tuning high-performing SOFC-cathode. ECS Trans 72:81–92
43. Yang G, Su C, Chen Y et al (2015) Cobalt-free SrFe<inf>0.9</inf>Ti<inf>0.1</inf>O<inf>3-δ</inf> as a high-performance electrode material for oxygen reduction reaction on doped ceria electrolyte with favorable CO<inf>2</inf> tolerance. J Eur Ceram Soc 35:2531–2539
44. Filatova EO, Egorova YV, Galdina KA et al (2017) Effect of Fe content on atomic and electronic structure of complex oxides Sr(Ti, Fe)O3 − δ. Solid State Ionics 308:27–33
45. Mroziński A, Molin S, Karczewski J et al (2019) The influence of iron doping on performance of $SrTi_{1-x}Fe_xO_{3-\delta}$ perovskite oxygen electrode for SOFC. ECS Trans 91:1299–1307
46. Wan TH, Saccoccio M, Chen C, Ciucci F (2015) Influence of the discretization methods on the distribution of relaxation times deconvolution: implementing radial basis functions with DRTtools. Electrochim Acta 184:483–499
47. Ciucci F, Chen C (2015) Analysis of electrochemical impedance spectroscopy data using the distribution of relaxation times: a Bayesian and hierarchical Bayesian approach. Electrochim Acta 167:439–454
48. Zheng K, Świerczek K, Polfus JM et al (2015) Carbon deposition and sulfur poisoning in SrFe<inf>0.75</inf>Mo<inf>0.25</inf>O<inf>3-δ</inf> and SrFe<inf>0.5</inf>Mn<inf>0.25</inf>Mo<inf>0.25</inf>O<inf>3-δ</inf> electrode materials for symmetrical SOFCs. J Electrochem Soc 162:F1078–F1087

49. Molin S, Gazda M, Jasinski P (2009) Conductivity improvement of $Ce_{0.8}Gd_{0.2}O_{1.9}$ solid electrolyte. J Rare Earths 27:655–660
50. Wang S, Kobayashi T, Dokiya M, Hashimoto T (2000) Electrical and ionic conductivity of Gd-doped ceria. J Electrochem Soc 147: 3606
51. Mogensen M, Sammes NM, Tompsett GA (2000) Physical, chemical and electrochemical properties of pure and doped ceria. Solid State Ionics 129:63–94
52. Hashim SS, Liang F, Zhou W, Sunarso J (2019) Cobalt-free perovskite cathodes for solid oxide fuel cells. ChemElectroChem:3549–3569
53. Riegraf M, Costa R, Schiller G et al (2019) Electrochemical impedance analysis of symmetrical Ni/gadolinium-doped ceria (CGO10) electrodes in electrolyte-supported solid oxide cells. J Electrochem Soc 166:F865–F872
54. Boukamp BA, Rolle A (2018) Use of a distribution function of relaxation times (DFRT) in impedance analysis of SOFC electrodes. Solid State Ionics 314:103–111
55. Clematis D, Barbucci A, Presto S et al (2019) Electrocatalytic activity of perovskite-based cathodes for solid oxide fuel cells. Int J Hydrog Energy 44:6212–6222
56. Dogdibegovic E, Guan W, Yan J et al (2016) Activity and stability of (Pr1-xNdx)2NiO4 as cathodes for solid oxide fuel cells: II. Electrochemical performance and performance durability. J Electrochem Soc 163:F1344–F1349
57. Merkle R, Maier J (2008) How is oxygen incorporated into oxides? A comprehensive kinetic study of a simple solid-state reaction with SrTiO3 as a model material. Angew Chem Int Ed 47:3874–3894
58. Rothschild A, Menesklou W, Tuller HL, Ivers-Tiffée E (2006) Electronic structure, defect chemistry, and transport properties of SrTi 1-xFe xO 3-y solid solutions. Chem Mater 18:3651–3659
59. Jung W, Tuller HL (2009) Impedance study of SrTi(1-x)Fe(x)O(3-delta) (x=0.05 to 0.80) mixed ionic-electronic conducting model cathode. Solid State Ionics 180:843–847
60. Metlenko V, Jung W, Bishop SR, Tuller HL, de Souza RA (2016) Oxygen diffusion and surface exchange in the mixed conducting oxides SrTi1-: YFeyO3- δ. Phys Chem Chem Phys 18(42):29495–29505
61. Samson A, Sogaard M, Knibbe R, Bonanos N (2011) High performance cathodes for solid oxide fuel cells prepared by infiltration of La[sub 0.6]Sr[sub 0.4]CoO[sub 3 - delta] into Gd-doped ceria. J Electrochem Soc 158:B650–B659
62. Hjalmarsson P, Søgaard M, Mogensen M (2008) Electrochemical performance and degradation of (La0.6Sr0.4)0.99CoO3 - δ as porous SOFC-cathode. Solid State Ionics 179:1422–1426
63. Ju J, Xie Y, Wang Z et al (2016) Electrical performance of nanostructured La0.6Sr0.4Co0.2Fe0.8O3-δ impregnated onto yttria-stabilized zirconia backbone. J Electrochem Soc 163:F393–F400
64. Cheng Y, Yu AS, Li X et al (2016) Preparation of SOFC cathodes by infiltration into LSF-YSZ composite scaffolds. J Electrochem Soc 163:F54–F58